AIAA JOURNAL
Vol. 44, No. 2, February 2006

Prediction Method for Broadband Noise from Unsteady Flow in a Slat Cove

Anurag Agarwal* and Philip J. Morris†
Pennsylvania State University, University Park, Pennsylvania 16802

Noise from high-lift devices such as slats and flaps can contribute significantly to the overall aircraft sound pressure levels, particularly during approach. The acoustic spectrum of the noise radiated from slats exhibits two distinct features. There is a high-frequency tonal noise component and a high-energy broadband component ranging from low- to midfrequencies. The objective is to predict the broadband slat noise. The broadband noise is predicted using a two-step process. First, the noise sources are modeled based on the local turbulence information. Then, the sound from these sources is propagated by assuming that the flow past the wing is uniform. A boundary element method is used to find Green's function for wave propagation in a moving medium in the presence of the wing. The noise in the far field is then predicted by forming a convolution of Green's function with the modeled sources. The attractive feature of this prediction scheme is the quick computational time, which makes it suitable for new design and control strategies.

I. Introduction

THE deployment of high-lift devices, namely, slats and flaps, is essential for aerodynamic reasons. However, such devices can significantly increase the aircraft airframe noise. This is the noise generated by the nonpropulsive components of the vehicle. The major components of airframe noise in an approach configuration are flap side edge, slat, and landing gear noise. Figure 1 from Guo et al.[1] and presented herein shows the noise spectra for different wing components of an MD 11 aircraft. Note that the noise from the slat and the flap dominates the noise spectrum. For newer aircraft such as the Boeing 777, slats generate even more noise compared to the other wing components.[1] Thus, the noise contribution from the slat is an important component of the total radiated noise during approach. In general, slat noise has two components, a high-frequency tonal noise signature and a broadband noise spectrum covering the lower and mid frequencies. It has been observed in experiments that the tonal noise emanates from a region in the vicinity of the slat trailing edge, whereas the broadband noise originates from the unsteady flow in the slat-cove region. The tonal noise generation mechanism has been investigated by several authors in the past. (See, for example, Khorrami et al.,[2] Tam and Pastouchenko,[3] and Agarwal and Morris.[4]) The objective of the present research is to develop a noise prediction scheme for the broadband noise.

Steady increases in aircraft operations have had a significant impact on community noise, especially close to airports. The problem is expected to become more acute in the future. Increasing noise has impacted airport operations, expansions, and their overall economics. Also, noise regulations are scheduled to become more stringent in the next few years. This means that aircraft of the future will have to be significantly quieter. This would require a significant noise reduction from all of the noise producing components. Thus, noise considerations and predictions must become a part of the overall aircraft design process, not an afterthought. However, for a noise prediction scheme to be a feasible tool in new design and control strategies, it must not only be reasonably accurate but should also have a short turnaround time. To predict noise accurately from fluctuations in an unsteady flow, complete information of the flow turbulence is desirable. This can be obtained by a direct numerical solver (DNS). However, DNS is restricted by computational resources to low-Reynolds-number simulations and is not an option for the extremely high Reynolds numbers encountered at aircraft operating conditions. Even a large-eddy simulation on commonly available parallel computers has a turnaround time of several days for high-Reynolds-number flow noise predictions. The proposed noise prediction scheme presented in this paper accepts some compromises in accuracy, but this is compensated for by improved computational efficiency. The scheme is developed with the aim of assisting design and control technologies by providing a reasonable noise estimate in a relatively short time.

A set of slat noise experiments were conducted by the Boeing Airplance Company at NASA Langley Research Center's Low Turbulence Pressure Tunnel (LTPT) on the scaled high-lift wing section shown in Fig. 2 (Ref. 5). A small-aperture microphone array was used to measure high-frequency noise and a larger-aperture microphone array measured low- to midfrequency noise. The measured acoustic spectrum is shown in Fig. 3. Besides the high-frequency tonal noise, the measured spectrum showed high sound pressure levels for a broad range of the frequency spectrum ranging from low to mid frequencies. The acoustic amplitudes in the lower-frequency range increased considerably with decreasing angle of attack. The same observation was made in the experimental investigations of Dobrzynski and Pott-Pollenske.[6] Paschal et al.[7] used particle image velocimetry (PIV) to map the flowfield on a McDonnell Douglas aircraft high-lift system in the NASA Langley Research Center LTPT. At low angles of attack (4 deg), they observed that large spanwise vortex structures emerged from the slat cove and were pumped through the gap between the slat and the main element. As the angle of attack was increased, the unsteadiness through the gap was reduced significantly. Similar observations were made by Takeda et al.[8] using the PIV technique on a United Kingdom National High Lift Programme model at the University of Southampton (2.1×1.7 m) wind tunnel. Unsteady Reynolds-averaged Navier–Stokes (RANS) simulations performed by Khorrami et al.[2] revealed a recirculation zone in the slat-cove area. They observed an unsteady flow exhibiting a complex motion of vortices of various length scales in the cove region. Some of the vortex structures escaped through the slat gap, whereas the majority of the structures were trapped in a recirculation zone in the slat-cove area. The unsteadiness in

Presented as Paper 2004-854 at the AIAA 42nd Aerospace Sciences Meeting, Reno, NV, 5–8 January 2004; received 25 August 2004; revision received 31 May 2005; accepted for publication 29 August 2005.

*Graduate Research Assistant, Department of Aerospace Engineering; currently Postdoctoral Researcher, Engineering Department, Cambridge University, Trumpington Street, Cambridge, England CB2 1PZ, United Kingdom. Member AIAA.

†Boeing/A. D. Welliver Professor, Department of Aerospace Engineering. Fellow AIAA.

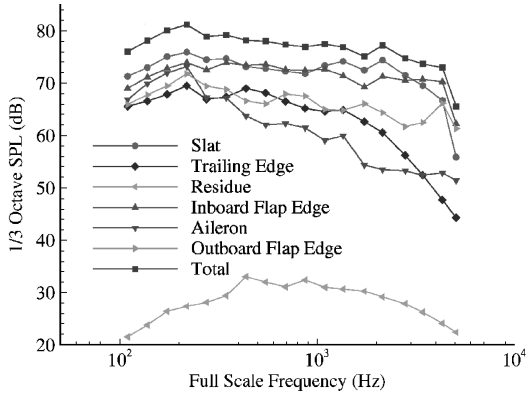

Fig. 1 Comparison of noise spectra from various wing components of model MD 11 aircraft (from Guo et al.[1]).

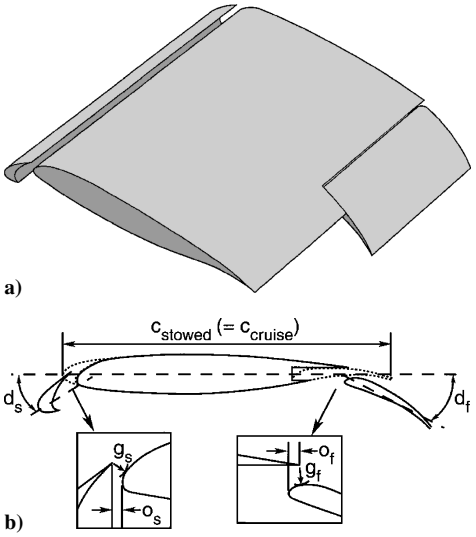

Fig. 2 Three-element high-lift system: a) three-dimensional model and b) cross-sectional view (from Khorrami et al.[5]).

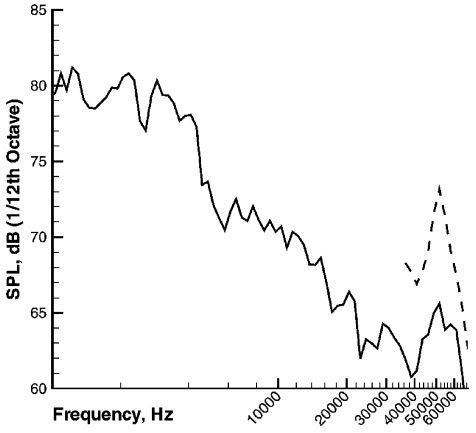

Fig. 3 Acoustic spectrum based on 1/12th octave bins with array focused on slat region, where configuration angle of attack is 9 deg, Reynolds number is 7.2 × 10⁶, and Mach number is 0.2; ——, low-frequency microphone array and – – –, high-frequency microphone array (from Khorrami et al.[2]).

the cove area decreased significantly with increasing slat deflection angle. This is in accord with the experimental observations. From these experimental and numerical investigations, it can be conjectured that there is a direct correlation between the unsteadiness in the slat-cove region and the radiated noise.

Various slat noise models have been proposed in the recent past. For example, Guo[9] has proposed a model based on the instability of the slat-cove region. Molin and Roger[10] attributed the slat broadband noise to the interaction of the turbulent structures from the slat-cove region with the leading edge of the main element. Dobrzynski and Pott-Pollenske[6] conjectured that the slat noise is a result of the interaction of the vortex structures originating from the unsteadiness from the slat-cove area with the slat trailing edge. They modeled this noise generation mechanism by a compact edge dipole. These simplistic models attempt to explore the physics of the slat noise generation process but cannot predict the slat noise itself to even within 10 dB of the observed sound pressure levels.

In this paper, the broadband noise emanating from the slat's cove region is predicted by coupling noise prediction from an acoustic analogy approach with a boundary element method (BEM). First the noise sources are modeled based on amplitude, length, and timescales obtained from an unsteady RANS simulation. Then the sound emitted from these sources is propagated through the mean flow into the far field, taking into account the scattering produced by the high-lift wing section. The noise-source model contains three empirical constants. These constants are determined by obtaining the best fit of the far-field noise prediction with the experimental data. This modeling procedure is similar to that used for jet noise predictions (cf. Morris and Farassat[11]). Once these constants are determined they can be used for other operating conditions and wing configurations. Manoha et al.[12] and Ostertag et al.[13] use a BEM with Lighthill's acoustic analogy to predict trailing-edge noise. There are two main differences between their formulation and the one presented in this paper. First, they have used an ordinary wave equation for noise propagation, whereas we have used a convective wave equation to account for mean-flow refraction effects. Second, we have modeled the noise sources by unsteady dilatations in contrast with the unsteady quadrupole terms used in Lighthill's acoustic analogy.

The method developed in this paper is for two-dimensional geometries. However, it can be extended to higher dimensions. The mean flow around the wing is assumed to be uniform. That is, the flow does not describe the actual mean flow in the presence of the wing. Rather, it is assumed that the mean flow is unaffected by the presence of the wing. Thus, the refraction effects due to the interaction of the acoustic waves with the nonuniform mean flow are ignored. The mean-flow refraction effects are not expected to be important because the wavelengths of the acoustic waves in the frequency range of interest are large compared to those in the region of nonuniformity. Furthermore, the experimental data are available at 270 deg (directly below the slat). At this angle, the refraction effects are expected to be negligible because the direction of sound propagation is approximately perpendicular to the direction of the flow.

The effect of acoustic scattering in the presence of a uniform mean flow is obtained by a BEM. The present noise prediction scheme has been developed with the objective of providing a viable prediction tool for new design and control strategies to reduce noise from high-lift devices. This requires a prediction tool that is fast and reliable over a range of input parameters. The BEM is more efficient compared to traditional finite difference (FD) or finite volume (FV) schemes. This is because the BEM allows for selective point-wise computation of the acoustic field as opposed to having to calculate the flowfield in the entire domain of interest as is required by FD and FV methods. Also, because the acoustic field in the BEM is obtained based only on the knowledge of the boundary field, there is no need to generate grids for the entire domain, which can be a tedious process for surfaces with complex geometries. Furthermore, the Sommerfeld radiation boundary conditions for outgoing waves are satisfied implicitly in the BEM formulation. Hence, no absorbing boundary conditions are required. For these reasons, the BEM is considered an appropriate prediction tool for the study of design and control strategies.

The BEM is formulated by first finding an expression for Green's function for a point source in a uniform mean flow in the presence of scattering bodies. This leads to a boundary-integral equation. This equation is discretized by dividing the boundary of the scattering bodies into elements, which leads to a set of equations for the unknown acoustic field at the boundary elements. These equations are solved to determine the acoustic field at the boundary. Then the

contributions from all of the boundary elements are added to find the acoustic field at a particular observer location. Finally, the noise in the far field is predicted by forming a convolution of Green's function with the modeled sources.

The rest of the paper is organized as follows. In Sec. II, an expression for the time-harmonic Green's function in the presence of a uniform mean flow and a scattering body is derived. This leads to a boundary integral equation. A BEM is developed to solve this equation in Sec. III. In Sec. IV, some simple examples of acoustic scattering are presented to validate the BEM. The noise prediction scheme is described in Sec. V. Numerical predictions using noise souces modeled from unsteady RANS calculations, the Green's function derived using BEM, and comparisons with experiments, where available, are presented in Sec. VI.

II. Green's Function for Convected Wave Equation in Presence of Solid Body

The two-dimensional time-harmonic Green's function $G(\boldsymbol{x};\omega)$ for the convected wave equation in the presence of a solid body satisfies the following differential equation:

$$\left[\left(-ik+M\frac{\partial}{\partial x}\right)^2-\nabla^2\right]c^2G(\boldsymbol{x}|\boldsymbol{x}_s)=\delta(\boldsymbol{x}-\boldsymbol{x}_s) \tag{1}$$

with the boundary condition, on S,

$$\frac{\partial G}{\partial \eta}=0 \tag{2}$$

where $\boldsymbol{x}_s$ is the source location, $k=\omega/c$, c is the freestream speed of sound, $M=u/c$, u is the uniform mean velocity in the streamwise x direction, S defines the boundary, and ξ and η are curvilinear orthogonal coordinates that represent the tangential and normal directions on S, respectively (Fig. 4).

To obtain this Green's function, first a generalized Green's theorem is derived. The free-space adjoint Green's function g^* satisfies the following differential equation:

$$\left[\left(-ik-M\frac{\partial}{\partial x}\right)^2-\nabla^2\right]c^2g^*(\boldsymbol{x}|\boldsymbol{x}_0)=\delta(\boldsymbol{x}-\boldsymbol{x}_0) \tag{3}$$

Taking the difference between the product of Eq. (1) with g^* and Eq. (3) with G yields

$$g^*(\boldsymbol{x}|\boldsymbol{x}_0)\delta(\boldsymbol{x}-\boldsymbol{x}_s)-G(\boldsymbol{x}|\boldsymbol{x}_s)\delta(\boldsymbol{x}-\boldsymbol{x}_0)=\nabla\cdot\boldsymbol{P}(G,g^*) \tag{4}$$

where

$$\boldsymbol{P}(G,g^*)=c^2\left\{\left[\left(g^*\frac{\partial G}{\partial x}-G\frac{\partial g^*}{\partial x}\right)M^2-2ikMGg^*\right]\boldsymbol{e}_x-(g^*\nabla G-G\nabla g^*)\right\} \tag{5}$$

and $\boldsymbol{e}_x$ is the unit vector in the x direction.

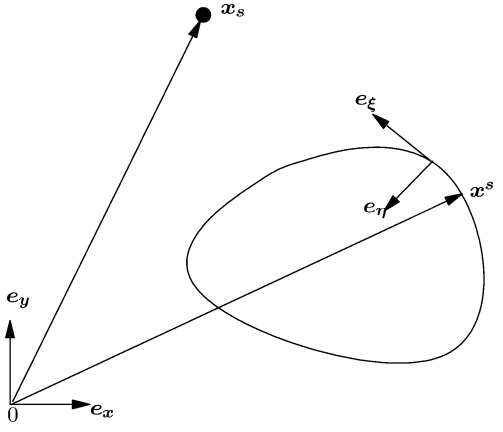

Fig. 4 Coordinate systems: (x, y), Cartesian and (ξ, η), body-fitted orthogonal curvilinear.

The integration of Eq. (4) over the region outside S and the application of the divergence theorem yields

$$G(\boldsymbol{x}_0|\boldsymbol{x}_s)=g^*(\boldsymbol{x}_s|\boldsymbol{x}_0)-\oint_S\boldsymbol{P}\left[G\left(\boldsymbol{x}^s\middle|\boldsymbol{x}_s\right),g^*\left(\boldsymbol{x}^s\middle|\boldsymbol{x}_0\right)\right]\cdot\boldsymbol{e}_\eta\,\mathrm{d}S \tag{6}$$

where $\boldsymbol{e}_\eta$ is the unit-normal vector at the point $\boldsymbol{x}^s$ on the surface S. By replacement of the dummy variable $\boldsymbol{x}_0$ with $\boldsymbol{x}$ and the use of the reciprocity relation $g^*(\boldsymbol{x}^s|\boldsymbol{x})=g(\boldsymbol{x}|\boldsymbol{x}^s)$, where $g(\boldsymbol{x}|\boldsymbol{x}_s)$ is the free-space Green's function derived in Appendix A, Eq. (6) can be written as

$$G(\boldsymbol{x}|\boldsymbol{x}_s)=g(\boldsymbol{x}|\boldsymbol{x}_s)-\oint_S\boldsymbol{P}\left[G\left(\boldsymbol{x}^s\middle|\boldsymbol{x}_s\right),g(\boldsymbol{x}|\boldsymbol{x}^s)\right]\cdot\boldsymbol{e}_\eta\,\mathrm{d}S \tag{7}$$

Now,

$$\frac{\partial G}{\partial x}=\frac{\partial G}{\partial \eta}\eta_x+\frac{\partial G}{\partial \xi}\eta_y \tag{8}$$

where $\eta_x=\boldsymbol{e}_\eta\cdot\boldsymbol{e}_x$ and $\eta_y=\boldsymbol{e}_\eta\cdot\boldsymbol{e}_y$. From the boundary condition, $\partial G(\boldsymbol{x}^s)/\partial\eta=0$. Then, Eq. (7) yields

$$G(\boldsymbol{x}|\boldsymbol{x}_s)=g(\boldsymbol{x}|\boldsymbol{x}_s)+c^2\oint_S\left(\left\{\left[-g(\boldsymbol{x}|\boldsymbol{x}^s)\frac{\partial G\left(\boldsymbol{x}^s\middle|x_s\right)}{\partial\xi}\eta_y+G\left(\boldsymbol{x}^s\middle|\boldsymbol{x}_s\right)\frac{\partial g(\boldsymbol{x}|\boldsymbol{x}^s)}{\partial x^s}\right]M^2+2ikMg(\boldsymbol{x}|\boldsymbol{x}^s)G\left(\boldsymbol{x}^s\middle|\boldsymbol{x}_s\right)\right\}\eta_x-G\left(\boldsymbol{x}^s\middle|\boldsymbol{x}_s\right)\frac{\partial g(\boldsymbol{x}|\boldsymbol{x}^s)}{\partial\eta}\right)\mathrm{d}S \tag{9}$$

This is the expression for Green's function in the presence of a solid body and a uniform mean flow. This equation contains $G(\boldsymbol{x}^s|\boldsymbol{x}_s)$ on the right-hand side, which is an unknown. In the following section, this unknown boundary function is calculated by the BEM.

III. Boundary Element Formulation

The boundary integral equation is given by

$$\left.\begin{matrix}G\left(\boldsymbol{x}=\boldsymbol{x}^s\middle|\boldsymbol{x}_s\right)/2\\ G(\boldsymbol{x}|\boldsymbol{x}_s)\end{matrix}\right\}=g(\boldsymbol{x}|\boldsymbol{x}_s)+c^2\oint_S\left\{\left(\left[-g(\boldsymbol{x}|\boldsymbol{x}^s)\frac{\partial G\left(\boldsymbol{x}^s\middle|\boldsymbol{x}_s\right)}{\partial\xi}\eta_y+G\left(\boldsymbol{x}^s\middle|\boldsymbol{x}_s\right)\frac{\partial g(\boldsymbol{x}|\boldsymbol{x}^s)}{\partial x^s}\right]M^2+2ikMg(\boldsymbol{x}|\boldsymbol{x}^s)G\left(\boldsymbol{x}^s\middle|\boldsymbol{x}_s\right)\right)\eta_x-G\left(\boldsymbol{x}^s\middle|\boldsymbol{x}_s\right)\frac{\partial g(\boldsymbol{x}|\boldsymbol{x}^s)}{\partial\eta}\right\}\mathrm{d}S \tag{10}$$

Here $G(\boldsymbol{x}^s|\boldsymbol{x}_s)$ and $G(\boldsymbol{x}|\boldsymbol{x}_s)$ are the unknowns. The first of these equations is derived from Eq. (9) in the limit $\boldsymbol{x}\to\boldsymbol{x}_s$. It is used to calculate $G(\boldsymbol{x}^s|\boldsymbol{x}_s)$ on the surface, which is then used to evaluate the surface integrals in the second equation to solve for G at an arbitrary observer location $\boldsymbol{x}$ for a given source location $\boldsymbol{x}_s$.

The reason that $\lim_{x\to x^s}G(\boldsymbol{x}|\boldsymbol{x}_s)\neq G(\boldsymbol{x}^s|\boldsymbol{x}_s)$ is that the surface integral on the right-hand side of Eqs. (10) is discontinuous in the limit. This is explained in Appendix B. The boundary element formulation for an ordinary wave equation is well known and avialable in several books (for example, Ref. 14). Equation (10) provides the boundary integral equation for the convected wave equation.

The integrals in Eqs. (10) are discretized by representing the surface S by a set of linear panels S_j (Fig. 5), such that

$$S=\sum_{j=1}^{n}S_j \tag{11}$$

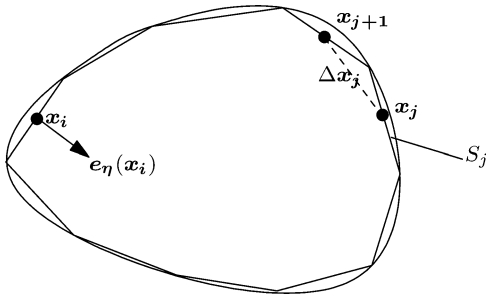

Fig. 5 Surface discretization for BEM.

On each panel S_j, the unknown surface functions are approximated by constants. That is,

$$G(\boldsymbol{x}^s) = G(\boldsymbol{x}_j) \tag{12}$$

$$\frac{\partial G(\boldsymbol{x}^s)}{\partial \xi} = \frac{\partial G(\boldsymbol{x}_j)}{\partial \xi} = \frac{G(\boldsymbol{x}_{j+1}) - G(\boldsymbol{x}_{j-1})}{|\boldsymbol{x}_{j+1} - \boldsymbol{x}_{j-1}|} \tag{13}$$

where $\boldsymbol{x}_j$ is the midpoint of the panel S_j. Hence, the first of Eqs. (10) can be written as

$$\frac{G(\boldsymbol{x}_i)}{2} = g(\boldsymbol{x}_i|\boldsymbol{x}_s) + c^2 \sum_{j=1}^{n} \left[-M^2 \eta_{x_j} \eta_{y_j} \frac{G(\boldsymbol{x}_{j+1}) - G(\boldsymbol{x}_{j-1})}{|\boldsymbol{x}_{j+1} - \boldsymbol{x}_{j-1}|} \right.$$

$$\times \int_{S_j} g\left(\boldsymbol{x}_i \middle| \boldsymbol{x}^s\right) \mathrm{d}S + M^2 \eta_{x_j} G(\boldsymbol{x}_j) \int_{S_j} \frac{\partial g\left(\boldsymbol{x}_i \middle| \boldsymbol{x}^s\right)}{\partial x^s} \mathrm{d}S$$

$$\left. + 2ikM\eta_{x_j} G(\boldsymbol{x}_j) \int_{S_j} g\left(\boldsymbol{x}_i \middle| \boldsymbol{x}^s\right) \mathrm{d}S - G(\boldsymbol{x}_j) \int_{S_j} \frac{\partial g\left(\boldsymbol{x}_i \middle| \boldsymbol{x}^s\right)}{\partial \eta} \mathrm{d}S \right]$$

where $\eta_{x_j} = \eta_x(\boldsymbol{x}_j)$. Equation (14) can be cast in the following matrix form

$$M_{ij} G_j = \boldsymbol{F}_i \tag{14}$$

where

$$M_{ij} = \frac{1}{2}\delta_{ij} - c^2 \left[-M^2 \left(\eta_{x_{j-1}} \eta_{y_{j-1}} \frac{I_{ij-1}}{\Delta \boldsymbol{x}_{j-1}} - \eta_{x_{j+1}} \eta_{y_{j+1}} \frac{I_{ij+1}}{\Delta \boldsymbol{x}_{j+1}} \right) \right.$$

$$\left. + M^2 \eta_{x_j} J_{ij} + 2ikM\eta_{x_j} I_{ij} - K_{ij} \right]$$

$$\boldsymbol{F}_i = g(\boldsymbol{x}_i|\boldsymbol{x}_s), \qquad G_j = G(\boldsymbol{x}_j), \qquad I_{ij} = \int_{S_j} g\left(\boldsymbol{x}_i \middle| \boldsymbol{x}^s\right) \mathrm{d}S$$

$$J_{ij} = \int_{S_j} \frac{\partial g\left(\boldsymbol{x}_i \middle| \boldsymbol{x}^s\right)}{\partial x^s} \mathrm{d}S, \qquad K_{ij} = \int_{S_j} \frac{\partial g\left(\boldsymbol{x}_i \middle| \boldsymbol{x}^s\right)}{\partial \eta} \mathrm{d}S$$

$$\delta_{ij} = \begin{cases} 0, & i \neq j \\ 1, & i = j \end{cases}$$

$$\Delta \boldsymbol{x}_j = |\boldsymbol{x}_{j+1} - \boldsymbol{x}_{j-1}|$$

$$\frac{\partial g\left(\boldsymbol{x}_i \middle| \boldsymbol{x}^s\right)}{\partial x^s} = \frac{i\gamma^3 k}{4c^2} \left\{ iM H_0^{(1)}\left[k\gamma\rho\left(\boldsymbol{x}_i, \boldsymbol{x}^s\right)\right] + \frac{\gamma\left(x_i - x^s\right)}{\rho\left(\boldsymbol{x}_i, \boldsymbol{x}^s\right)} \right.$$

$$\left. \times H_1^{(1)}\left[k\gamma\rho\left(\boldsymbol{x}_i, \boldsymbol{x}^s\right)\right] \right\} \exp\left[-ik\gamma^2 M\left(x_i - x^s\right)\right]$$

$$\frac{\partial g\left(\boldsymbol{x}_i \middle| \boldsymbol{x}^s\right)}{\partial y^s} = \frac{i\gamma^2 k}{4c^2} \left\{ \frac{y_i - y^s}{\rho\left(\boldsymbol{x}_i, \boldsymbol{x}^s\right)} H_1^{(1)}\left[k\gamma\rho\left(\boldsymbol{x}_i, \boldsymbol{x}^s\right)\right] \right\}$$

$$\times \exp\left[-ik\gamma^2 M\left(x_i - x^s\right)\right]$$

$$\rho\left(\boldsymbol{x}_i, \boldsymbol{x}^s\right) = \sqrt{\gamma^2\left(x_i - x^s\right)^2 + \left(y_i - y^s\right)^2} \tag{15}$$

The integrals in Eqs. (15) can be evaluated using a standard Gaussian quadrature when $i \neq j$. When $i = j$, we have, on S_j, $\boldsymbol{x}^s = (x_j + \xi\eta_{y_j}, y_j - \xi\eta_{x_j})$. Thus,

$$\left.\begin{aligned} x_i - x^s &= x_j - x^s = -\xi\eta_{y_j} \\ y_i - y^s &= y_j - y^s = \xi\eta_{x_j} \end{aligned}\right\} \left(-|S_j/2| \leq \xi \leq |S_j/2|\right) \tag{16}$$

$$\int_{S_j} (\,)\,\mathrm{d}S = \int_{-|S_j|/2}^{|S_j|/2} (\,)\,\mathrm{d}\xi \tag{17}$$

By the use of Eqs. (16) and (17), the integrals in Eqs. (15) can be written, after some manipulation, as

$$I_{jj} = \frac{i\gamma}{4c^2} \int_{-|S_j|/2}^{|S_j|/2} H_0^{(1)}\left(k\gamma\mu_j|\xi|\right) \exp\left(ik\gamma^2 M\eta_{y_j}\xi\right) \mathrm{d}\xi$$

$$= \frac{i\gamma}{2c^2} \int_0^{|S_j|/2} \Lambda(\xi)\,\mathrm{d}\xi$$

$$J_{jj} = \frac{i\gamma^3 k}{2c^2} \int_0^{|S_j|/2} \left[iM\Lambda(\xi) - i\frac{\gamma\eta_{y_j}}{\mu_j}\Omega(\xi) \right] \mathrm{d}\xi$$

$$K_{jj} = \frac{ik\gamma^2}{2c^2} \int_0^{|S_j|/2} \left[i\gamma M\eta_x \Lambda(\xi) - i\frac{\gamma^2\eta_{x_j}\eta_{y_j} - \eta_{x_j}\eta_{y_j}}{\mu_j}\Omega(\xi) \right] \mathrm{d}\xi$$

$$\Lambda(\xi) = H_0^{(1)}(k\gamma\mu_j\xi)\cos\left(k\gamma^2 M\eta_{y_j}\xi\right)$$

$$\Omega(\xi) = H_1^{(1)}(k\gamma\mu_j\xi)\sin\left(k\gamma^2 M\eta_{y_j}\xi\right) \tag{18}$$

where $\mu_j = (\gamma^2\eta_{y_j}^2 + \eta_{x_j}^2)^{1/2}$. Note that

$$\int_0 \Lambda(\xi)\,\mathrm{d}\xi$$

has a logarithmic endpoint singularity. This integral can be evaluated by a generalized Gaussian quadrature for logarithmic functions. (See Ma et al.[15] for details.) On substitution of the expressions for J_{jj} and K_{jj} in M_{jj}, note that the terms involving $\Omega(\xi)$ are eliminated. Hence, the $\Omega(\xi)$ integrals are not evaluated.

The sound pressure on the surface $G(\boldsymbol{x}^s)$ can now be evaluated by inverting the matrix in Eq. (14). Finally, the sound pressure at an arbitrary observer location $G(\boldsymbol{x})$ is calculated using the lower equation in Eqs. (10) and the now known surface values of $G(\boldsymbol{x}^s)$. The numerical discretization of this equation leads to the right-hand side of Eq. (14) with $\boldsymbol{x}_i$ replaced with $\boldsymbol{x}$. Note that now all of the integrals are regular and can be evaluated using a standard Gaussian quadrature.

IV. Examples of Application of BEM

In this section, some examples are presented to validate the BEM code for simply and multiply connected domains. Also, the effect of a mean flow on the directivity pattern is shown. Comparisons are made with analytical solutions when they are available.

A. Simply Connected Domains

As an example of the application of the BEM to simply connected domains, the canonical problem of the scattering of acoustic waves from a point source by a cylinder is solved. A schematic of the problem considered here is shown in Fig. 6. The radius of the cylinder is 1 m and its center is at (0, 0). A line source of frequency 200 rad/s is placed at (20, 0). Figure 7 shows the predicted directivity pattern at a radius of 100 m. The analytical solution for this problem is readily available, for example, see Morse and Ingard.[16] A surface resolution of eight points per wavelength is found to be adequate to yield a converged solution. However, at low frequencies, when

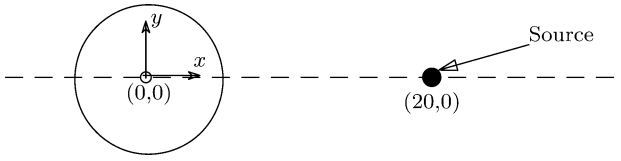

Fig. 6 Schematic for acoustic scattering from cylinder.

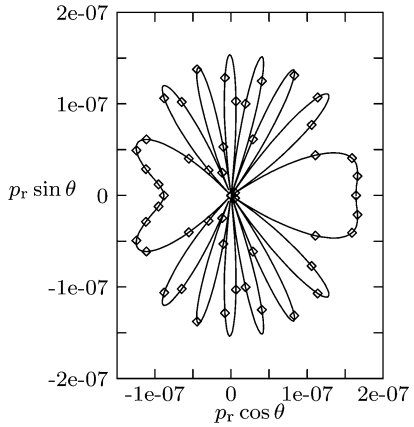

Fig. 7 Sound directivity patterns for scattering of acoustic waves from line source at (20, 0) by a cylinder centered at (0, 0), source frequency is 200 rad/s: ——, BEM solution and ◇, analytical solution.

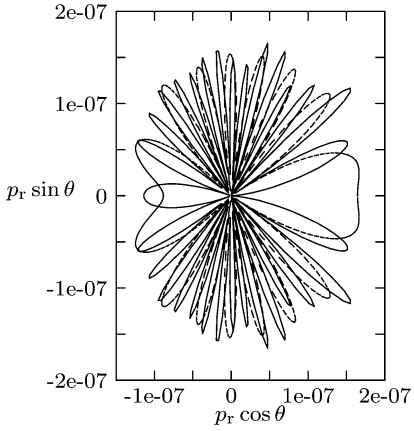

Fig. 8 Comparison of sound directivity patterns for scattering of acoustic waves from line source by a cylinder: – – –, $M = 0$ and ——, $M = 0.2$.

the acoustic wavelength is large or comparable to the dimension of the surface, more points need to be used to resolve the geometry. For example, for the present example, eight points per wavelenght corresponds to only four surface grid points. Figure 7 shows the BEM solution obtained by discretizing the surface by 25 elements. Note that it agrees well with the analytical solution.

The effect of a mean flow on the sound directivity patterns is shown in Fig. 8, which compares the directivity patterns for no mean flow and in the presence of a uniform mean flow of Mach number 0.2. Note that the directivity is altered significantly compared to the no-flow case. In general, the mean-flow effects on the directivity depend on several factors such as observer distance, source frequency, and Mach number; however, it is important to account for the mean flow because it is difficult to know a priori whether the mean flow is going to impact the acoustic directivity significantly.

B. Multiconnected Domains

The application of the BEM to multiconnected domains is more relevant to the problem of slat-noise prediction because the exterior domain of a multielement high-lift wing is multiconnected. The BEM can be applied to multiconnected domains by defining the surface S in the surface integral of Eqs. (10) to include the boundaries of all surfaces, even though they may be disjoint, such that each surface is traversed in a counterclockwise direction. For example, consider the two disjoint surfaces, S_1 and S_2, shown in Fig. 9. The domains Ω_1 and Ω_2 can be made simply connected by adding lines l_1 and l_2, such that $\lim_{\epsilon\to 0} l_1 = -l_2$, where ϵ is the separation between the two lines. Thus, the surface integral in Eqs. (10) can be written as

$$\oint_S = \int_{S_1-\epsilon} + \int_{S_2-\epsilon} + \int_{l_1} + \int_{l_2} \tag{19}$$

However, in the limit $\epsilon \to 0$,

$$\int_{l_1} = -\int_{l_2}$$

Therefore,

$$\oint_S = \sum_{i=1}^{2} \oint_{S_i} \tag{20}$$

As a test case, the problem of the scattering of acoustic waves from a line source by two cylinders is solved. The two cylinders, A of radius 0.5 m and B of radius 0.25 m, are located at $(-4, 0)$ and $(4, 0)$, respectively, as shown in Fig. 10. A line source of frequency 8720 rad/s is located at the origin. For the BEM solution, the surface of each cylinder is discretized by 30 elements. This is a computational aeroacoustics benchmark problem, and its analytical solution has been provided by Sherer.[17] In Fig. 11, the rms pressure values obtained by the BEM solver are compared with the analytical solution along the x axis for $-9 \le x \le 9$. Figure 11 shows good agreement between the analytical and the numerical solutions.

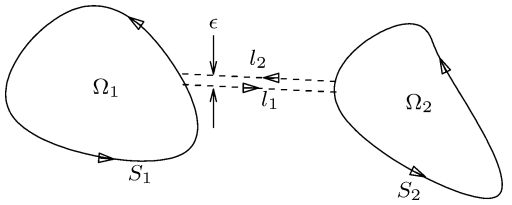

Fig. 9 Multiconnected domain $\Omega = \Omega_1 \cup \Omega_2$.

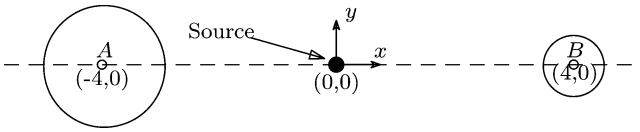

Fig. 10 Schematic for acoustic scattering from two cylinders.

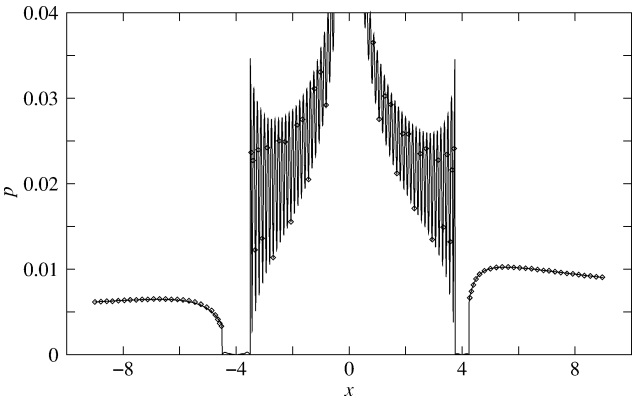

Fig. 11 RMS pressure for scattering of acoustic waves from a line source by two cylinders. ——, BEM solution and ◇, analytical solution.

V. Noise Prediction Scheme

Once the Green's function for wave propagation and the noise source terms are known, the acoustic field can be obtained by a straightforward convolution of Green's function with the sources. The sources are modeled here on the basis of the acoustic analogy proposed by Morris and Farassat.[11] If the inviscid compressible equations of motion for a perfect gas are linearized about a mean flow, which is assumed to be known, the resulting equations can be written

$$\frac{\mathrm{D}\pi'}{\mathrm{D}t} + \frac{\partial u_i'}{\partial x_i} = \theta(\boldsymbol{x}, t) \tag{21}$$

$$\frac{\mathrm{D}u_i'}{\mathrm{D}t} + c^2\frac{\partial \pi'}{\partial x_i} = -f_i(\boldsymbol{x}, t) \tag{22}$$

where, in the present case of a uniform mean flow,

$$\frac{\mathrm{D}}{\mathrm{D}t} = \frac{\partial}{\partial t} + \bar{u}\frac{\partial}{\partial x_1} \tag{23}$$

$$\pi = \frac{1}{\gamma}\,\ell_n\left(\frac{p}{p_0}\right) \tag{24}$$

and $\pi' = \pi - \bar{\pi} = p'/\gamma p_0$. Here, p_0 is the constant mean static pressure, overbars denote mean quantities, and primes denote fluctuations about that mean. Here $\theta(\boldsymbol{x}, t)$ and $f_i(\boldsymbol{x}, t)$ are equivalent sources, $\theta(\boldsymbol{x}, t)$ is a dilatation rate source, and $f_i(\boldsymbol{x}, t)$ is an equivalent acceleration. An additional equivalent source associated with fluctuations in the sound speed has been neglected in Eq. (22) because it is only expected to be important in heated turbulent flows. Morris and Boluriaan[18] have shown that the far-field noise prediction formulas are the same whether the dilatation rate or acceleration sources are considered. Note, however, that the directivities of the different representations of the source are different. In the present case, the focus is on the measured spectrum at 90 deg to the flow direction where the different source descriptions give identical results. Thus, for simplicity, only the dilatation rate source will be included in the subsequent analysis. From Eqs. (21) and (22), and for a constant speed of sound c, we obtain

$$\frac{\mathrm{D}^2 p'}{\mathrm{D}t^2} - c^2\nabla^2 p' = \rho^2 c^2\frac{\mathrm{D}\theta}{\mathrm{D}t} \tag{25}$$

Let Green's function for this convected wave equation satisfy

$$\left(\frac{\mathrm{D}^2}{\mathrm{D}t^2} - c^2\nabla^2\right)G(\boldsymbol{x}, t|\boldsymbol{x}_s, t_s) = \delta(\boldsymbol{x} - \boldsymbol{x}_s)\delta(t - t_s) \tag{26}$$

and the time-harmonic Green's function is related to $G(\boldsymbol{x}, t|\boldsymbol{x}_s, t_s)$ by

$$G(\boldsymbol{x}, t|\boldsymbol{x}_s, t_s) = \frac{1}{2\pi}\int_{-\infty}^{\infty} G(\boldsymbol{x}|\boldsymbol{x}_s; \omega)\exp[-i\omega(t - t_s)]\,\mathrm{d}\omega \tag{27}$$

Then

$$p'(\boldsymbol{x}, t) = \frac{\rho c^2}{2\pi}\iiint_S \mathrm{d}\boldsymbol{x}_s \int_{-\infty}^{\infty}\mathrm{d}t_s \int_{-\infty}^{\infty} G(\boldsymbol{x}|\boldsymbol{x}_s; \omega)$$

$$\times\ \exp[-i\omega(t - t_s)]\frac{\mathrm{D}\theta(\boldsymbol{x}_s, t_s)}{\mathrm{D}t_s}\,\mathrm{d}\omega \tag{28}$$

where

$$\frac{\mathrm{D}}{\mathrm{D}t_s} = \frac{\partial}{\partial t_s} + \bar{u}\frac{\partial}{\partial x_{1_s}} \tag{29}$$

Now the spectral density is given by

$$S(\boldsymbol{x}, \omega) = \int_{-\infty}^{\infty} < p'(\boldsymbol{x}, t)p'(\boldsymbol{x}, t + \tau) > e^{i\omega\tau}\,\mathrm{d}\tau \tag{30}$$

Thus,

$$S(\boldsymbol{x}, \omega) = \frac{\rho^2 c^4}{4\pi^2}\iiint_S \mathrm{d}\boldsymbol{x}_2 \iiint_S \mathrm{d}\boldsymbol{x}_1 \int_{-\infty}^{\infty}\cdots\int G(\boldsymbol{x}|\boldsymbol{x}_1; \omega_1)$$

$$\times\ G(\boldsymbol{x}|\boldsymbol{x}_2; \omega_2)\left\langle\frac{\mathrm{D}\theta(\boldsymbol{x}_1, t_1)}{\mathrm{D}t_1}\frac{\mathrm{D}\theta(\boldsymbol{x}_2, t_2)}{\mathrm{D}t_2}\right\rangle\exp[-i\omega_1(t - t_1)$$

$$- i\omega_2(t - t_2) - i\omega_2\tau]e^{i\omega\tau}\,\mathrm{d}\tau\,\mathrm{d}\omega_1\,\mathrm{d}\omega_2\,\mathrm{d}t_1\,\mathrm{d}t_2 \tag{31}$$

The integration with respect to τ can be performed immediately because

$$\int_{-\infty}^{\infty}\exp[i(\omega - \omega_2)\tau]\,\mathrm{d}\tau = 2\pi\delta(\omega - \omega_2) \tag{32}$$

Then

$$S(\boldsymbol{x}, \omega) = \frac{\rho^2 c^4}{2\pi}\iiint_S \mathrm{d}\boldsymbol{x}_2 \iiint_S \mathrm{d}\boldsymbol{x}_1 \int_{-\infty}^{\infty}\cdots\int G(\boldsymbol{x}|\boldsymbol{x}_1; \omega_1)$$

$$\times\ G(\boldsymbol{x}|\boldsymbol{x}_2; \omega_2)\left\langle\frac{\mathrm{D}\theta(\boldsymbol{x}_1, t_1)}{\mathrm{D}t_1}\frac{\mathrm{D}\theta(\boldsymbol{x}_2, t_2)}{\mathrm{D}t_2}\right\rangle\exp[-i(\omega_1 + \omega_2)t$$

$$+ i\omega_1 t_1 + i\omega_2 t_2]\delta(\omega - \omega_2)\,\mathrm{d}\omega_1\,\mathrm{d}\omega_2\,\mathrm{d}t_1\,\mathrm{d}t_2 \tag{33}$$

Now we assume that the space–time correlation is only a function of separation distance $\boldsymbol{\eta} = \boldsymbol{x}_2 - \boldsymbol{x}_1$ and time delay $\tau = t_2 - t_1$. Then the integration with respect to t_2 can be replaced by integration with respect to τ. We also note that

$$\left\langle\frac{\mathrm{D}\theta(\boldsymbol{x}_1, t_1)}{\mathrm{D}t_1}\frac{\mathrm{D}\theta(\boldsymbol{x}_2, t_2)}{\mathrm{D}t_2}\right\rangle = \frac{\mathrm{D}^2}{\mathrm{D}t_1\mathrm{D}t_2}\langle\theta(\boldsymbol{x}_1, t_1)\theta(\boldsymbol{x}_2, t_2)\rangle \tag{34}$$

with $\langle\theta(\boldsymbol{x}_1, t_1)\theta(\boldsymbol{x}_2, t_2)\rangle = R_\theta(\boldsymbol{\eta}, \tau)$ and

$$\frac{\mathrm{D}^2}{\mathrm{D}t_1\mathrm{D}t_2} = -\left(\frac{\partial}{\partial\tau} + \bar{u}\frac{\partial}{\partial\xi}\right)^2 = -\frac{\mathrm{D}^2}{\mathrm{D}\tau^2} \tag{35}$$

where $\boldsymbol{\eta} = (\xi, \eta, \zeta)$. Then

$$S(\boldsymbol{x}, \omega) = -\frac{\rho^2 c^4}{2\pi}\iiint_S \mathrm{d}\boldsymbol{x}_2 \iiint_S \mathrm{d}\boldsymbol{x}_1 \int_{-\infty}^{\infty},\ldots,\int G(\boldsymbol{x}|\boldsymbol{x}_1; \omega_1)$$

$$\times\ G(\boldsymbol{x}|\boldsymbol{x}_2; \omega_2)\frac{\mathrm{D}^2 R_\theta(\boldsymbol{\eta}, \tau)}{\mathrm{D}\tau^2}\exp[-i(\omega_1 + \omega_2)t$$

$$+ i(\omega_1 + \omega_2)t_1 + i\omega_2\tau]\delta(\omega - \omega_2)\,\mathrm{d}\omega_1\,\mathrm{d}\omega_2\,\mathrm{d}t_1\,\mathrm{d}\tau \tag{36}$$

The integrations with respect to t_1, ω_1, and ω_2 can now be performed because

$$\int_{-\infty}^{\infty} e^{i(\omega_1 + \omega_2)t_1}\,\mathrm{d}t_1 = 2\pi\delta(\omega_1 + \omega_2). \tag{37}$$

Then,

$$S(\boldsymbol{x}, \omega) = -\rho^2 c^4\iiint_S \mathrm{d}\boldsymbol{x}_1 \iiint_S \mathrm{d}\boldsymbol{\eta}\int_{-\infty}^{\infty} G(\boldsymbol{x}|\boldsymbol{x}_1; -\omega)$$

$$\times\ G(\boldsymbol{x}|\boldsymbol{x}_1 + \boldsymbol{\eta}; \omega)\frac{\mathrm{D}^2 R_\theta(\boldsymbol{\eta}, \tau)}{\mathrm{D}\tau^2}\exp(i\omega\tau)\,\mathrm{d}\tau \tag{38}$$

To be consistent with the assumption of a uniform mean flow it will be assumed that

$$R_\theta(\boldsymbol{\eta}, \tau) = A\left(m^4/\tau_s^2\right)$$

$$\times\exp\left[-(\xi - \bar{u}\tau)^2/l_s^2 - \eta^2/l_s^2 - \zeta^2/l_z^2 - \tau^2/\tau_s^2\right] \tag{39}$$

where τ_s, l_s, and l_z are the characteristic source timescales and length scales in the x and y and z directions, respectively. Here $m = u_s/c$, where u_s is the source characteristic velocity. Because

$$\frac{\mathrm{D}}{\mathrm{D}\tau} = \frac{\partial}{\partial\tau} + \bar{u}\frac{\partial}{\partial\xi} \tag{40}$$

$$\frac{\mathrm{D}^2}{\mathrm{D}\tau^2} R_\theta(\boldsymbol{\eta}, \tau) = \frac{\partial^2}{\partial\tau^2} R_\theta(\boldsymbol{\eta}, \tau) \tag{41}$$

Then integration by parts yields

$$S(\boldsymbol{x}, \omega) = \rho^2 c^4 \omega^2 \iiint_S \mathrm{d}\boldsymbol{x}_1 \iiint_S \mathrm{d}\boldsymbol{\eta} \int_{-\infty}^{\infty} G(\boldsymbol{x}|\boldsymbol{x}_1; -\omega)$$

$$\times G(\boldsymbol{x}|\boldsymbol{x}_1 + \boldsymbol{\eta}; \omega) R_\theta(\boldsymbol{\eta}, \tau) \exp(i\omega\tau)\, \mathrm{d}\tau \tag{42}$$

To proceed further, it is necessary to provide a relationship between the two closely spaced Green's functions. In an unbounded medium, a simple phase relationship can be postulated for all frequencies. However, due to the multiple reflections in the propagation path for the slat noise sources, no such relationship can be provided in general. Thus, the sources will be assumed to be compact. That is, $\omega l_s/c \ll 1$. Then Green's functions can be taken as identical over the source correlation volume and because

$$G(\boldsymbol{x}|\boldsymbol{x}_1; -\omega) = G^*(\boldsymbol{x}|\boldsymbol{x}_1; \omega) \tag{43}$$

where the asterisk denotes the complex conjugate,

$$S(\boldsymbol{x}, \omega) = \rho^2 c^4 \omega^2 \iiint_S \mathrm{d}\boldsymbol{x}_1 \int_{-\infty}^{\infty} \cdots \int |G(\boldsymbol{x}|\boldsymbol{x}_1; \omega)|^2$$

$$\times \exp\left[-\frac{(\xi - \bar{u}\tau)^2}{l_s^2} - \frac{\eta^2}{l_s^2} - \frac{\zeta^2}{l_z^2}\right] A \frac{m^4}{\tau_s^2} \exp\left(-\frac{\tau^2}{\tau_s^2} + i\omega\tau\right)$$

$$\times \mathrm{d}\tau\, \mathrm{d}\xi\, \mathrm{d}\eta\, \mathrm{d}\zeta \tag{44}$$

Now,

$$\int_{-\infty}^{\infty}\int_{-\infty}^{\infty} \exp\left(-\frac{\eta^2}{l_s^2}\right) \exp\left(-\frac{\zeta^2}{l_z^2}\right) \mathrm{d}\eta\, \mathrm{d}\zeta = \pi l_s l_z \tag{45}$$

The integrations with respect to ξ and τ can also be performed analytically to yield

$$S(\boldsymbol{x}, \omega) = \rho^2 c^4 \omega^2 \pi^2 \iiint_S |G(\boldsymbol{x}|\boldsymbol{x}_1; \omega)|^2$$

$$\times A \frac{m^4}{\tau_s} l_s^2 l_z \exp\left(-\frac{\omega^2\tau^2}{4}\right) \mathrm{d}\boldsymbol{x}_1 \tag{46}$$

Now, let

$$l_s = c_l\sqrt{\kappa}\,/\omega, \qquad \tau_s = c_\tau(1/\omega), \qquad u_s = (2\kappa/3)^{\frac{1}{2}} \tag{47}$$

where κ and ω are the averaged turbulence kinetic energy and specific dissipation rate that are obtained from the k–ω model used in the RANS calculations, and c_l, c_τ are the parameters of the model. Also, for convenience, let $l_z = l_s$. This has no effect on the shape of the predicted spectrum. Then, finally, the spectral density is given by

$$S(\boldsymbol{x}, \omega) = \frac{4\pi^2}{9} A \frac{c_l^3}{c_\tau^3} \iiint_S |G(\boldsymbol{x}|\boldsymbol{x}_1; \omega)|^2$$

$$\times \kappa^{\frac{7}{2}} \omega^2 \tau_s^2 \exp\left(\frac{-\omega^2\tau_s^2}{4}\right) \mathrm{d}\boldsymbol{x}_1 \tag{48}$$

VI. Results

The prediction of the spectral density $S(\boldsymbol{x}, \omega)$ as given by Eq. (48) requires a solution for Green's function $G(\boldsymbol{x}|\boldsymbol{x}_1)$ for the pressure field from a point source in the cove region $\boldsymbol{x}_1$ at an observer location $\boldsymbol{x}$ and the values of the three parameters of the model given in Eq. (47). Green's function is obtained by using the boundary element formulation described in Sec. III. The geometry of the three-element wing used for the present simulations is shown in Fig. 12. The wing surface is discretized to have eight elements per acoustic wavelength. This surface resolution has been found to be adequate to yield a converged solution for Green's function. Figure 13 shows the directivity pattern at a radius of 1.82 m from a point source placed in the slat-cove region at (0, 0). The frequency of the point source is 2000 Hz. Clearly, Fig. 13 represents Green's function for a particular source location and frequency. In general, the directivity pattern is a function of frequency and can vary significantly from one source location to another. Thus, observations based on a single directivity plot cannot be generalized to other frequencies or source locations. It is the combined effect of all of the source locations at various frequencies that describes the noise spectrum as given by Eq. (48). To obtain the integral in Eq. (48), Green's functions are calculated for all source locations in the slat-cove region. We interpolated the source data from the RANS solution on a 51×51 grid. This grid size yielded a converged solution. Approximately 2 min per frequency is required to compute Green's functions for all source locations. The turbulence field in the vicinity of the wing is obtained from the k–ω model-based unsteady RANS simulation by Khorrami et al.[2] The turbulence kinetic energy values in the vicinity of the slat are shown in Fig. 14. The data have been normalized with the freestream speed of sound for the velocity scale and the clean chord length for the length scale. Note that the strongest turbulent fluctuations are confined to the slat-cove region.

The three empirical constants c_l, c_τ, and A are, in general, chosen to obtain the best fit to the experimental data. The following values are selected for these parameters:

$$c_l = 0.256, \qquad c_\tau = 0.05, \qquad A = 0.6 \tag{49}$$

To test the importance of scattering effects from the wing geometry, the noise spectrum is first predicted by ignoring the presence

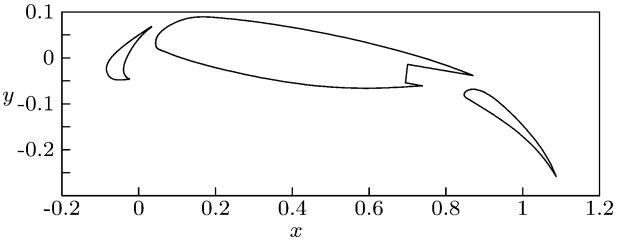

Fig. 12 Surface definition of wing geometry for BEM.

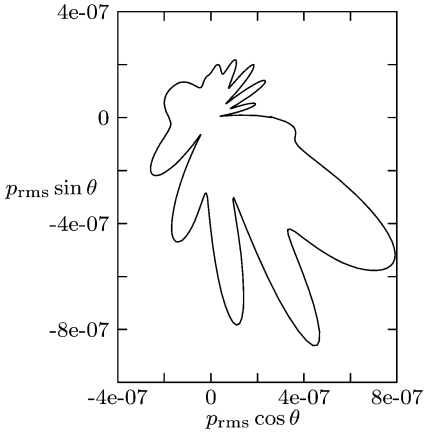

Fig. 13 Directivity pattern at radius of 1.82 m from point source of frequency 2000 Hz in slat-cove region.

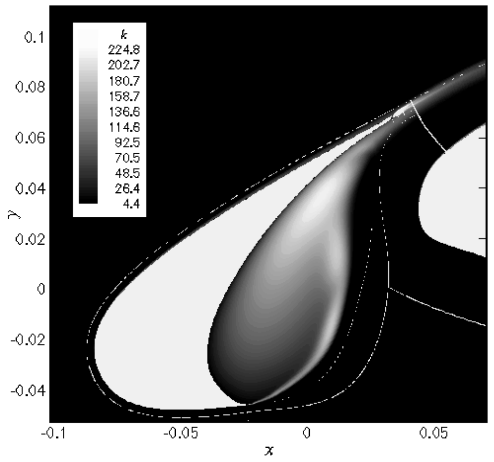

Fig. 14 Contour plot of turbulence kinetic energy in vicinity of slat.

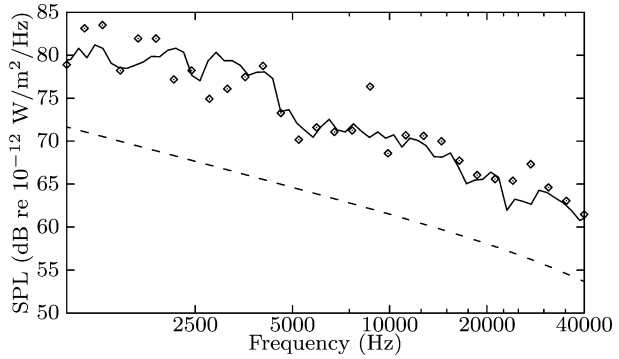

Fig. 15 Comparison with experimental data of predicted spectral density at 270 deg to downstream direction: ——, experiment, Khorrami et al.[2]; ◇, prediction with the wing; and – – –, prediction without the wing.

of the wing. Again, Eq. (48) is used to predict the spectral density in the absence of the wing but with $G(\boldsymbol{x}|\boldsymbol{x}_1;\omega)$ replaced with the free-space Green's function $g(\boldsymbol{x}|\boldsymbol{x}_1;\omega)$ given in Appendix A. The same values for the empirical constants given in Eq. (49) are chosen for this prediction model.

Figure 15 shows a comparison of the calculated noise spectra using the present prediction schemes with the experimental measurement at 270 deg (directly beneath the slat). Note that the predicted noise spectrum in the presence of the wing compares well with the measured spectrum. The predicted noise is approximately within 5 dB of the measured noise levels over the entire frequency spectrum. The prediction made in the absence of the wing captures the spectral shape, but underestimates the sound pressure levels. Thus, at 270 deg, acoustic scattering from the wing enhances the acoustic radiation significantly but does not modify the spectral shape of the radiated acoustic intensity significantly.

Figure 16 shows a comparison of the predicted noise spectra both with and without the wing for three different observer locations. Note that for an upstream location of 210 deg the sound pressure levels are significantly lower than at 270 or 310 deg. This is because the noise sources in the slat-cove region are not in a direct line of sight with the observer at the 210-deg location. Thus, the slat serves as an acoustic shield, which creates a shadow zone in the upstream direction. Not surprisingly, the predictions made in the absence of the wing are unable to capture this variation of sound pressure level as a function of observer location. Thus, acoustic scattering by the wing is important for the calculation of sound pressure levels at all frequencies.

Figure 17 shows a comparison of the noise spectra at 270 deg for predictions made with and without the mean flow. The combined effect of the mean flow and the wing is to increase the sound pressure levels slightly at all frequencies compared to the no-flow

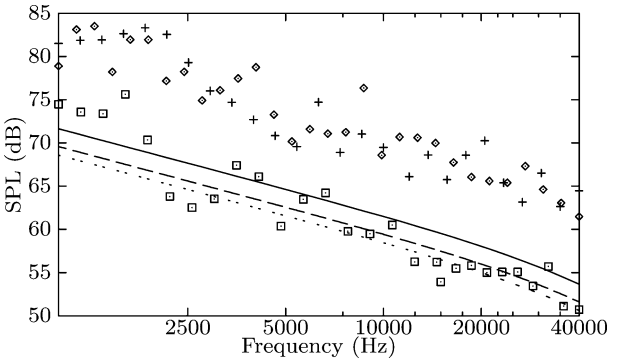

Fig. 16 Comparison of noise spectra at different observer locations, points represent predictions with wing: +, $\theta = 310$ deg; ◇, $\theta = 270$ deg; and ⊡, $\theta = 210$ deg; lines represent predictions without the wing: ——, $\theta = 270$ deg; – – –, $\theta = 310$ deg; and · · · ·, $\theta = 210$ deg.

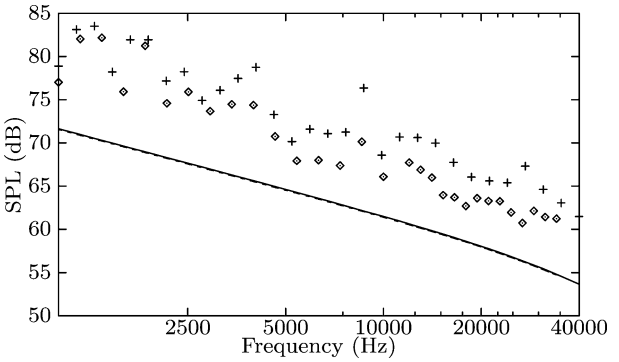

Fig. 17 Effect of mean flow on noise spectra at 270 deg: +, $M = 0.2$ prediction and ◇, $M = 0$ prediction, with wing; · · · ·, $M = 0.2$ prediction and – – –, $M = 0$ prediction, without wing.

case. The predictions made without the presence of the wing are similar because at 270 deg the mean-flow Mach number of 0.2 has a negligible effect on the free-space Green's function.

VII. Conclusions

A semi-empirical scheme has been presented to predict the broadband noise from slats. The broadband noise is predicted by a two-step process. First, the turbulent sources in the slat-cove region are modeled. Then the sound from these sources is propagated by the convected wave equation. The acoustic scattering produced by the geometry of the wing is accounted for by a BEM that has been developed to calculate Green's function for the noise propagation problem. The final noise prediction is obtained by forming a convolution of Green's function with modeled noise sources. The noise-source model has three empirical constants. These constants are chosen to obtain the best fit of the predicted noise with the experimental data. The predicted noise spectrum compares well with the available experimental measurements.

The noise prediction scheme requires as input the turbulence field quantities and at least one experimental measurement of the noise spectrum to calibrate the empirical constants. The turbulence field can be obtained by either a RANS solver, through experimental measurements, or by modeling the flowfield. The noise prediction scheme is semi-empirical but has improved efficiency compared to prediction methods based purely on computational aeroacoustics. The prediction scheme described in this paper has been developed with the objective of aiding new designs of high-lift wings to reduce airframe noise.

The present model for the source statistics is very crude, being homogeneous and Gaussian. This is a function of the lack of experimental data on the turbulence statistics in the slat-cove region. Though this could be obtained from numerical simulations, the statistics so produced are likely to be unrealistic unless all scales

of the turbulence motion are simulated. This is not possible for high-Reynolds-number flows. Thus, measurements of two-point statistics in the slat-cove region would provide valuable guidance for source modeling. In addition, acoustic spectra at different angles, in controlled conditions, are desirable. The majority of in-tunnel experiments have produced phased array data to avoid contamination by tunnel noise as well as to identify source locations. Though this is valuable for source identification, it makes calibration and validation of any noise prediction model difficult. The best solution would be to use available flyover data: However, this often uses the phased array technique as well. Also, the three-dimensional nature of the actual slat installation makes predictions with the present two-dimensional model more problematic. In any event, it is hoped that the present method will provide a framework for future studies of broadband slat noise.

Appendix A: Free-Space Green's Function: Time-Harmonic Point Source in Uniform Mean Flow

The two-dimensional Green's function for a time-harmonic point source placed in a uniform mean flow is described by

$$\left(\frac{\partial}{\partial t}+\bar{u}\frac{\partial}{\partial x}\right)^2 g(\boldsymbol{x}|\boldsymbol{x}_s)-c^2\nabla^2 g(\boldsymbol{x}|\boldsymbol{x}_s) = \delta(x-x_s)\delta(y-y_s)\exp[-i\omega t] \tag{A1}$$

In the limit $t\to\infty$, the response is governed by

$$\left(-i\omega+\bar{u}\frac{\partial}{\partial x}\right)^2 g(\boldsymbol{x}|\boldsymbol{x}_s)-c^2\nabla^2 g(\boldsymbol{x}|\boldsymbol{x}_s)=\delta(x-x_s)\delta(y-y_s) \tag{A2}$$

This equation can be rearranged to give

$$\left(-ik+M\frac{\partial}{\partial x}\right)^2 g(\boldsymbol{x}|\boldsymbol{x}_s)-\nabla^2 g(\boldsymbol{x}|\boldsymbol{x}_s)=\frac{1}{c^2}\delta(x-x_s)\delta(y-y_s) \tag{A3}$$

where $k=\omega/c$. Let $\bar{g}=g/\exp[-ik\gamma^2 Mx]$, where $\gamma=1/\sqrt{(1-M^2)}$. This transforms Eq. (A3) into

$$-\frac{1}{\gamma^4}\frac{\partial^2\bar{g}}{\partial x^2}-k^2\bar{g}-\frac{1}{\gamma^2}\frac{\partial^2\bar{g}}{\partial y^2}=\frac{\exp[ik\gamma^2 Mx]}{c^2\gamma^2}\delta(x-x_s)\delta(y-y_s) \tag{A4}$$

Using the coordinate transformations $\bar{x}=\gamma^2 x$, $\bar{y}=\gamma y$, we obtain

$$-k^2\bar{g}-\bar{\nabla}^2\bar{g}=\frac{\exp[ikM\bar{x}]}{c^2\gamma^2}\delta\left(\frac{\bar{x}}{\gamma^2}-x_s\right)\delta\left(\frac{\bar{y}}{\gamma}-y_s\right) \tag{A5}$$

where $\bar{\nabla}^2=\partial^2/\partial\bar{x}^2+\partial^2/\partial\bar{y}^2$. With the properties of the delta function

$$\delta(x-a)\phi(x)=\delta(x-a)\phi(a) \tag{A6}$$

$$\delta(x/a)=a\delta(x) \tag{A7}$$

Eq. (A5) can be written as

$$(-k^2-\bar{\nabla}^2)\bar{g}(\bar{\boldsymbol{x}}|\bar{\boldsymbol{x}_s})=\exp(ikM\bar{x}_s)(\gamma/c^2)\delta(\bar{x}-\bar{x}_s)\delta(\bar{y}-\bar{y}_s) \tag{A8}$$

The operator on the left-hand side is the familiar Helmholtz operator, Green's function for which is known. Thus,

$$\bar{g}(\bar{\boldsymbol{x}}|\bar{\boldsymbol{x}_s})=(i\gamma/4c^2)\exp[ikM\bar{x}_s]H_0^{(1)}\left[k\sqrt{(\bar{x}-\bar{x}_s)^2+(\bar{y}-\bar{y}_s)^2}\right] \tag{A9}$$

Transforming back to the original variables, the free-space Green's function is given by

$$g(x,y|x_s,y_s)=(i\gamma/4c^2)\exp[-ik\gamma^2 M(x-x_s)] \times H_0^{(1)}\left[k\gamma\sqrt{\gamma^2(x-x_s)^2+(y-y_s)^2}\right] \tag{A10}$$

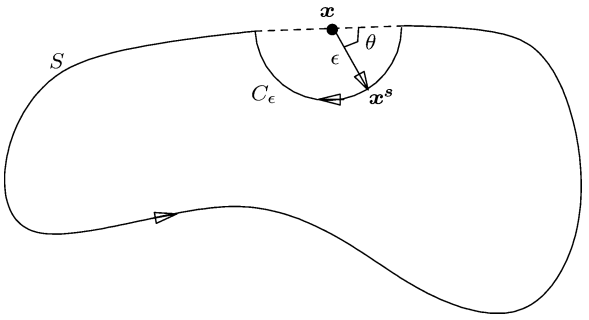

Fig. B1 Surface deformation such that in limit $\epsilon\to 0, x\to x^s$.

Appendix B: Surface Integral Discontinuity in Boundary Element Formulation

The surface integral in Eq. (10) can be evaluated in the limit $\boldsymbol{x}\to\boldsymbol{x}^s$ by selecting a point $\boldsymbol{x}$ on the surface but deforming the surface in a semicircle C_ϵ of radius ϵ below $\boldsymbol{x}$, as shown in Fig. B1. Then, in the limit $\epsilon\to 0$, $\boldsymbol{x}\to\boldsymbol{x}^s$. Let

$$s(\boldsymbol{x})=c^2\oint_S\left(\left\{\left[-g(\boldsymbol{x}|\boldsymbol{x}^s)\frac{\partial G(\boldsymbol{x}^s|\boldsymbol{x}_s)}{\partial\xi}\eta_y+G(\boldsymbol{x}^s|\boldsymbol{x}_s)\frac{\partial g(\boldsymbol{x}|\boldsymbol{x}^s)}{\partial x^s}\right]M^2 + 2ikMg(\boldsymbol{x}|\boldsymbol{x}^s)G(\boldsymbol{x}^s|\boldsymbol{x}_s)\right\}\eta_x-G(\boldsymbol{x}^s|\boldsymbol{x}_s)\frac{\partial g(\boldsymbol{x}|\boldsymbol{x}^s)}{\partial\eta}\right)\mathrm{d}S = \oint_S\Psi(\boldsymbol{x}|\boldsymbol{x}^s)\,\mathrm{d}S \tag{B1}$$

With the surface S defined as in Fig. B1,

$$s(\boldsymbol{x})=\int_{S-2\epsilon}\Psi(\boldsymbol{x}|\boldsymbol{x}^s)\,\mathrm{d}S+\int_{C_\epsilon}\Psi(\boldsymbol{x}|\boldsymbol{x}^s)\,\mathrm{d}S \tag{B2}$$

It can be shown that in the limit $\epsilon\to 0$, the $g(\boldsymbol{x},\boldsymbol{x}^s)$ terms in $\Psi(\boldsymbol{x}|\boldsymbol{x}^s)$ do not contribute to the

$$\int_{C_\epsilon}$$

integral. Then, after some simple manipulations, the integral over C_ϵ can be written as

$$\lim_{\epsilon\to 0}\int_{C_\epsilon}\Psi(\boldsymbol{x}|\boldsymbol{x}^s)\,\mathrm{d}S=-c^2G(\boldsymbol{x}^s|\boldsymbol{x}_s)\int_{C_\epsilon}\left[\frac{\partial g(\boldsymbol{x}|\boldsymbol{x}^s)}{\partial x^s}\eta_x(1-M^2) + \frac{\partial g(\boldsymbol{x}|\boldsymbol{x}^s)}{\partial y^s}\eta_y\right]\mathrm{d}\boldsymbol{x}^s \tag{B3}$$

On the curve C_ϵ, $\boldsymbol{x}-\boldsymbol{x}^s=-\epsilon\boldsymbol{e}_\eta$, $\mathrm{d}\boldsymbol{x}^s=\epsilon\,\mathrm{d}\theta$. On substitution of the expressions for the partial derivatives of the free-space Green's function [relations (15)], Eq. (B3) can be simplified to

$$\lim_{\epsilon\to 0}\int_{C_\epsilon}\Psi(\boldsymbol{x}|\boldsymbol{x}^s)\,\mathrm{d}S=-G(\boldsymbol{x}^s|\boldsymbol{x}_s)\frac{i\gamma^2 k}{4} \times\int_0^\pi\frac{(\boldsymbol{x}-\boldsymbol{x}^s)\cdot\boldsymbol{e}_\eta}{\rho(\boldsymbol{x},\boldsymbol{x}^s)}H_1^{(1)}[k\gamma\rho(\boldsymbol{x},\boldsymbol{x}^s)]\epsilon\,\mathrm{d}\theta \tag{B4}$$

where $\rho(\boldsymbol{x},\boldsymbol{x}^s)=\epsilon(\gamma^2\cos^2\theta+\sin^2\theta)^{1/2}$ and $H_n^{(1)}()$ represents a Hankel function of the first kind. Note that in the asymptotic limit for small ρ, the integrals involving the $H_0^{(1)}()$ functions evaluate to zero and are, hence, ignored. Using the asymptotic limit $H_1^{(1)}(\rho)\simeq -2i/(\pi\rho)$ for small ρ, and after some more manipulations, we obtain

$$\lim_{\epsilon\to 0}\int_{C_\epsilon}\Psi(\boldsymbol{x}|\boldsymbol{x}^s)\,\mathrm{d}S=G(\boldsymbol{x}^s|\boldsymbol{x}_s)\frac{\gamma}{2\pi}\int_0^\pi\frac{1}{\gamma^2\cos^2\theta+\sin^2\theta}\,\mathrm{d}\theta = \frac{G(\boldsymbol{x}^s|\boldsymbol{x}_s)}{2} \tag{B5}$$

Hence, from Eqs. (B1), (B2), and (B5),

$$\lim_{x \to x^s} s(\boldsymbol{x}) = s(\boldsymbol{x}^s) + G(\boldsymbol{x}^s)/2 \tag{B6}$$

Thus, in the limit $\boldsymbol{x} \to \boldsymbol{x}^s$, the surface integral has a jump of magnitude $G(\boldsymbol{x}^s)/2$. This explains the factor of one-half on the left-hand side of Eqs. (10) when the response is evaluated at the boundary.

Acknowledgments

This work has been supported by the NASA Langley Research Center under Grant NAG1-01-009, Technical Monitor Mehdi Khorrami. The authors thank M. R. Khorrami and M. Choudhari of NASA Langley Research Center for providing mean-flow data from their numerical calculations.

References

[1]Guo, Y. P., Yamamoto, K. J., and Stoker, R. W., "Component-Based Empirical Model for High-Lift System Noise Prediction," *Journal of Aircraft*, Vol. 40, No. 5, 2003, pp. 914–922.

[2]Khorrami, M. R., Singer, B. A., and Berkman, M. E., "Time-Accurate Simulations and Acoustic Analysis of Slat Free Shear Layer," *AIAA Journal*, Vol. 40, No. 7, 2002, pp. 1284–1291.

[3]Tam, C. K. W., and Pastouchenko, N., "Gap Tones," *AIAA Journal*, Vol. 39, No. 8, 2001, pp. 1442–1448.

[4]Agarwal, A., and Morris, P. J., "Investigation of the Physical Mechanisms of Tonal Sound Generation by Slats," AIAA Paper 2002-2575, 2002.

[5]Khorrami, M. R., Berkman, M. E., and Choudhari, M., "Unsteady Flow Computations of a Slat with a Blunt Trailing Edge," *AIAA Journal*, Vol. 38, No. 11, 2000, pp. 2050–2058.

[6]Dobrzynski, W., and Pott-Pollenske, M., "Slat Noise Source Studies for Farfield Noise Prediction," AIAA Paper 2001-2158, 2001.

[7]Paschal, K., Jenkins, L., and Yao, C., "Unsteady Slat-Wake Characteristics of a High-Lift Configuration," AIAA Paper 2000-0139, 2000.

[8]Takeda, K., Ashcroft, G. B., and Zhang, X., "Unsteady Aerodynamics of Slat Cove Flow in a High-Lift Device Configuration," AIAA Paper 2001-0706, 2001.

[9]Guo, Y. P., "A Model for Slat Noise Generation," AIAA Paper 97-1647, 1997.

[10]Molin, N., and Roger, M., "The Use of Amiet's Methods in Predicting the Noise from 2D High Lift Devices," AIAA Paper 2000-2064, 2000.

[11]Morris, P. J., and Farassat, F., "Acoustic Analogy and Alternative Theories for Jet Noise Prediction," *AIAA Journal*, Vol. 40, No. 4., 2002, pp. 671–680.

[12]Manoha, E., Elias, G., Troff, B., and Sagaut, P., "Towards the Use of Boundary Element Mehtod in Computational Aeroacoustics," AIAA Paper 99-1980, 1999.

[13]Ostertag, J., Celic, A., and Wagner, S., "Trailing-Edge Noise Prediction by SATIN on the Basis of Steady RANS Solutions," AIAA Paper 2002-2471, 2002.

[14]Chen, G., and Zhou, J., *Boundary Element Methods*, Academic Press, San Diego, CA, 1992.

[15]Ma, J., Rokhlin, V., and Wandzura, S., "Generalized Gaussian Quadrature Rules for Systems of Arbitrary Functions," *SIAM Journal on Numerical Analysis*, Vol. 33, No. 3, 1996, pp. 971–996.

[16]Morse, P. M., and Ingard, K. U., *Theoretical Acoustics*, Princeton Univ., Press, Princeton, NJ, 1986, Chap. 8.

[17]Sherer, S. E., "Multi-Geometry Scattering Problem," *4th Computational Aeroacoustics Workshop on Benchmark Problems*, NASA CP-2004-212954, 2004, pp. 39–43.

[18]Morris, P. J., and Boluriaan, S., "On the Prediction of Jet Noise From CFD Data," AIAA Paper 2004-2977, 2004.

J. Gore
Associate Editor